4-2021

Adsorption and Surface Diffusion of Metals on α-Al_2O_3 for Advanced Manufacturing Applications

Austin Biaggne
Boise State University

Gregory Noble
Boise State University

Lan Li
Boise State University

The version of record of this article, first published in *The Journal of The Minerals, Metals & Materials Society (TMS)*, is available online at Publisher's website: http://doi.org/10.1007/s11837-021-04589-y

JOM, Vol. 73, No. 4, 2021
https://doi.org/10.1007/s11837-021-04589-y

Adsorption and Surface Diffusion of Metals on α-Al_2O_3 for Advanced Manufacturing Applications

AUSTIN BIAGGNE ,[1,4] GREGORY NOBLE,[2] and LAN LI [1,3]

1.—Micron School of Materials Science and Engineering, Boise State University, Boise, ID 83725, USA. 2.—Departments of Physics, Boise State University, Boise, ID 83725, USA. 3.—Center for Advanced Energy Studies, Idaho Falls, ID 83401, USA. 4.—e-mail: austinbiaggne@u.boisestate.edu

The adsorption and diffusion of Mo and Nb adatoms on the α-Al_2O_3 (0001) surface were explored using density functional theory-based methods. Adsorption energies of Mo and Nb adatoms at minima sites on the surface were determined. Mo and Nb adatoms prefer to adsorb to the same locations on the surface, and larger adsorption energies calculated for Nb compared to Mo indicate that Nb adatom-surface interactions are stronger than Mo. Using minima adsorption sites as initial and final locations for surface diffusion, energy barriers for diffusion were calculated using the nudged elastic band method. Overall, Mo and Nb follow roughly the same diffusion paths. The diffusion pre-factors for Mo and Nb are similar; however, Mo diffusion has a lower energy barrier and thus a larger diffusion coefficient compared with Nb. These results provide insight into the role of surface diffusion of Mo and Nb adatoms during advanced manufacturing processes.

INTRODUCTION

Advanced manufacturing has been shown to be a viable method to build sensors for in-pile nuclear reactor applications, such as dosimeters,[1] melt wires,[2] and temperature sensors.[3] Advanced manufacturing methods, including aerosol jet printing (AJP) and plasma jet printing (PJP), are currently being developed as a means to build sensors and instrumentation that cannot be built with traditional techniques.[2,4] AJP utilizes aerosolized metal nanoparticles in an "ink" that is deposited on substrates in a focused manner. Once deposited, the metal nanoparticles are sintered together in an oven.[2] PJP is a similar process, which also uses metal ink. However, it allows for printing on flexible substrates.[5] The understanding of the metal printing process is necessary for the development of advanced manufacturing methods, and the diffusion mechanism of metal nanoparticles on the substrate surfaces plays a crucial role in the metal printing process[6,7] because it affects how the metal nanoparticles move and form on the substrates.[8] To determine the adsorption and diffusion mechanisms of printed metal atoms on substrates, computational methods are needed.

First-principles modeling methods have been commonly employed to study the metal-substrate interaction and the diffusion of metal nanoparticles on surfaces. Density functional theory (DFT)-based methods have been implemented to study bulk diffusion[9–12] and surface diffusion of adatoms.[13–16] Specifically, nudged elastic band (NEB) methods have been used to determine minimum energy pathways (MEP) and energy barriers of diffusion. The climbing-image (CI) version of NEB could also reveal the transition states of diffusion pathways. Milas et al.[14] used NEB and CI-NEB to determine the surface diffusion paths and diffusion pre-factors of Al, O, Pt, Hf, and Y on the alumina surfaces. In addition, Wu et al.[16] used similar approaches to study the diffusion paths and energetics of H on an alumina surface.

The goal of our study is to use advanced manufacturing to build a high-temperature irradiation-resistant thermocouple (HTIR-TC), which would allow for real-time temperature measurement in a nuclear reactor. A HTIR-TC, consisting of Mo and

(Received December 3, 2020; accepted February 5, 2021; published online February 25, 2021)

Nb,[17–19] offers the better balance of high temperature and irradiation resistance than traditional TC materials, such as Pt, Rh, and Ni alloys.[20] For example, Pt/Rh thermocouples are rated for temperatures up to 2093 K, and Pt and Rh have neutron capture cross sections of 10 and 150 barns, respectively.[21] Mo and Nb have higher melting temperatures (2883 K and 2743 K) and smaller neutron capture cross sections (2.65 and 1.15).[21] A common substrate used for printing is alumina (Al_2O_3).[22–24] The diffusion mechanisms of Mo and Nb on the alumina specifically at the atomistic level have not been fully addressed in either computational or experimental studies. Here, we utilized the NEB and CI-NEB methods to study the energetics and diffusion mechanisms of Mo and Nb adatoms on the α-Al_2O_3 (0001) surface. The surface energies of the α-Al_2O_3 (0001) with three different atomic layer terminations were estimated. Through the calculations of adsorption energies, favorable sites for the Mo and Nb adatoms on the surface were determined. Diffusion pathways between the energetically favorable adsorption sites were also determined using NEB. The MEP from the NEB calculations were then used as an input for the CI-NEB calculations to determine the diffusion energy barriers for the Mo and Nb adatoms on the α-Al_2O_3 (0001) surface. Finally, frequency calculations were employed to estimate diffusion coefficients.

COMPUTATIONAL METHODS

Density functional theory (DFT) with dipole corrections, as implemented in the Vienna Ab-initio Simulation Package (VASP)[25,26] software, was used. The projector augmented wave (PAW)[27,28] pseudopotentials were utilized along with the Perdew–Burke–Ernzerhof (PBE) form of the generalized gradient approximation (GGA).[29] For Al and O atoms, the electrons in valence states were treated explicitly, while the semi-core 4*p* electrons of Mo and Nb were not included in the frozen core. In the literature,[14,16,30–32] the α-Al_2O_3 (0001) surface has been extensively studied, and, as highlighted in Fig. 1a, there are three different atomic terminal layers (labeled as Al, Al′, and O). In our calculations, six stoichiometric layers (18 atomic layers) were used, and the bottom five atomic layers were frozen to simulate a bulk region. The structural relaxations were done with $4 \times 4 \times 1$ k-point sampling, a plane-wave energy cutoff of 600 eV, Gaussian smearing with 0.01 eV width, and a force convergence criterion of 0.01 eV/Å.

Initial and final locations of the diffusing adatoms were found via adsorption energy calculations. The adatoms were allowed to fully relax. In similar studies,[10,14,15] NEB was done between energetica minima sites to establish a MEP, from which single-image CI-NEB calculations were performed to speed up the convergence time, which has been shown to be sufficient for diffusion energy barrier calculations.[10,14,15,33] To determine diffusion energy barriers, five-image NEB calculations were performed between the adsorption sites with the lowest energy minimum for at least 30 ionic steps, which yielded the estimates of MEP between adsorption minima. From the MEP results, single-image CI-NEB calculations were performed to determine the transition state (TS) of the diffusing adatom. Upon the convergence of the CI-NEB calculations, the highest energy image was at a saddle point. A force convergence of 0.01 eV/Å was used for CI-NEB calculations. Once minimum and saddle point locations were determined, frequency calculations were performed to find the vibrational frequencies of the adatoms by displacing the adatoms with $\pm$ 0.02 Å. Like previous studies,[14] the adatoms were assumed to have a weak vibrational coupling with the surface, so the frequencies of the surface atoms were not considered.

RESULTS

Surface Energies

To determine the most energetically favorable surface of α-Al_2O_3 (0001), the energies of the Al, Al′, and O-terminated surfaces were calculated using the equation below:

$$E_{\text{surface}} = E_{\text{slab}} - \frac{N_{\text{slab}}\left(\frac{E_{\text{uc}}}{N_{\text{uc}}}\right)}{2A} \quad (1)$$

where E_{slab} is the total energy of the relaxed slab, N_{slab} is the number of atoms in the slab, E_{uc} is the total energy of the Al_2O_3 unit cell, N_{uc} is the number of atoms in the unit cell, and A is the area of the surface of the slab. A vacuum slab of 25 Å was used to form the α-Al_2O_3 (0001) surface.

The most energetically favorable surface is Al′-terminated, shown in Fig. 1, with an energy of 2.60 J/m^2, more than a half smaller than the values for O- and Al-terminated surfaces ($\sim$6 J/m^2). Upon the relaxation, on the Al′-terminated surface the Al′-O bond lengths are on average 1.70 Å, while the O-Al′-O angles are all 190°. In general, our results agree with previous computational[14,16,30,34–37] and experimental[38] studies. In addition, on the Al layer the bond lengths are about 1.81 Å between Al atoms and first-layer O atoms and 1.96 Å between Al atoms and second-layer O atoms. The O-Al-O bond angles are 97.6° for Al atoms and first-layer O atoms and 81.8° for Al atoms and second-layer O atoms. The Al′-terminated surface was used for subsequent adsorption and diffusion calculations, discussed below.

Adsorption Sites

Using the Al′-terminated surface, adsorption sites for Mo and Nb adatoms and associated energies were calculated. The adatoms were initialized on the high-symmetry positions of the unit cell, as

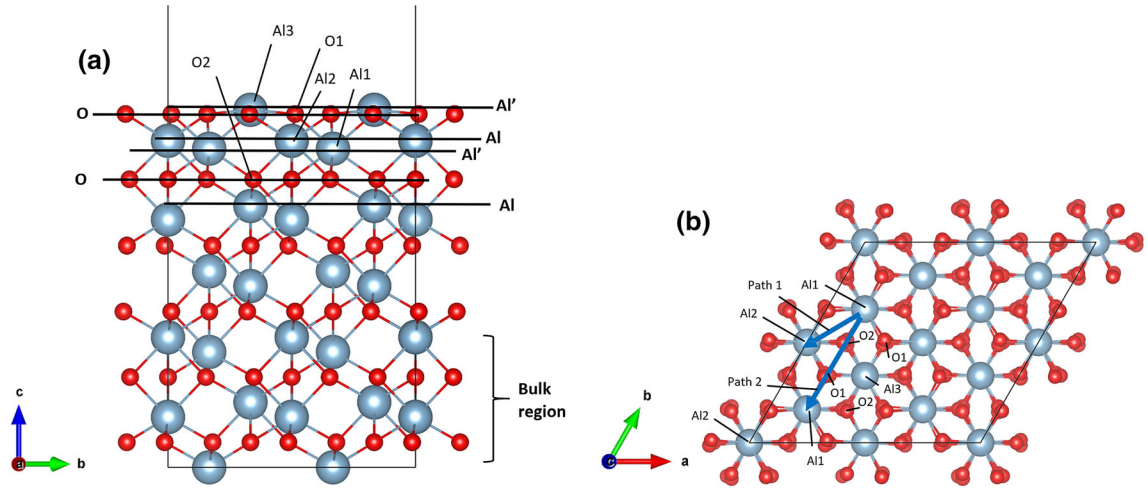

Fig. 1. (a) Relaxed 2 × 2 × 1 Al′-terminated α-Al_2O_3 (0001) slab with a vacuum slab above. The first six atomic layers (Al′, O, and Al) are labeled and denoted with horizontal black lines. Al1, Al2, Al3, O1, and O2 atoms are labeled for reference. (b) Relaxed 2 × 2 × 1 Al′-terminated α-Al_2O_3 (0001) surface. Initial adsorption locations are labeled as Al1, Al2, and Al3 for high-symmetry sites above Al atoms and O1 and O2 for high-symmetry sites above O atoms. Diffusion paths are labeled with arrows as path 1 (shorter arrow between Al1 and Al2 sites) or path 2 (longer arrow between Al1 sites). Al atoms are blue, and O atoms are red.

labeled in Fig. 1. They were also initially placed 2 Å above the surface and allowed to fully relax. It was found that Mo adatoms relaxed to be directly either above the Al2 site or slightly off the Al1 site (not directly above). Similarly, Nb adatoms preferentially relaxed to be right above either the Al1 or Al2 sites. Upon adsorption above the Al1 sites, the Mo adatom was about 1.68 Å above the surface while the Nb adatom was about 1.55 Å above the surface. Furthermore, the Al1 atoms moved downward into the bulk region by 0.13 Å and 0.20 Å to separate from Mo and Nb, respectively. Upon adsorption above the Al2 sites, the Mo adatom was 1.94 Å above the surface while the Nb was 1.63 Å above the surface. Similar to the Al1 sites, the Al2 atom moved downwards by 0.10 Å for Mo and 0.17 Å for Nb. The change in the layer morphology, including Al-O bond lengths and O-Al-O bond angles, was limited down to the third Al′ layer. We found no significant change beyond that compared to the relaxed structure before adsorption (Fig. 1a). This observation confirmed that the size of the slab we chose was converged for the adsorption and diffusion calculations.

To further study the adatom-surface bonding characteristics, the charge density difference was calculated, as below:

$$\Delta\rho = \rho_{\text{slab+adatom}} - \rho_{\text{slab}} - \rho_{\text{adatom}} \qquad (2)$$

where $\rho_{\text{slab+adatom}}$ is the electron density of the relaxed slab with the adatom on top, ρ_{slab} is the electron density of the slab, and ρ_{adatom} is the electron density of just the adatom alone. Results for the charge density differences are depicted in Fig. 2. Electron density accumulates between the Mo adatom and the Al atom Al3 (labeled in Fig. 1) as opposed to the O atoms surrounding the Al1 and Al2 sites, as seen in Fig. 2a and b. This indicates that Mo interacts preferentially with surface Al3 atoms, as opposed to the subsurface Al1 and Al2 atoms. Similarly, electron density also accumulates between the Nb adatoms and surface Al3 atoms, as shown in Fig. 2c and d. Due to the strong Mo- and Nb-surface interactions, we found that the Al3 atoms were moved upwards from the surface by 0.54 Å and 0.41 Å upon the adsorption of the Mo and Nb adatoms above Al1 sites, respectively. Similarly, the Al3 atoms were moved upwards by 0.10 Å and 0.40 Å upon the adsorption of the Mo and Nb adatoms above Al2 sites, respectively.

Corresponding adsorption energies were calculated to quantify the adatom-surface interaction using the equation, as below:

$$E_{\text{ads}} = -[E_{\text{slab+adatom}} - (E_{\text{slab}} + E_{\text{adatom}})] \qquad (3)$$

where $E_{\text{slab+adatom}}$ is the total energy of the relaxed slab and adatom system, E_{slab} is the total energy of the relaxed slab, and E_{adatom} is the formation energy of a single Mo or Nb atom. Adsorption energies that are more positive indicate a stronger adatom-surface interaction. Table I lists the adsorption energies of the Mo and Nb adatoms. In general, adsorption of adatoms above Al1 sites yields larger adsorption energies than those above Al2 sites. For adsorption above both Al1 and Al2 sites, Nb adatoms exhibit larger adsorption energies than Mo adatoms. Furthermore, the favorable adsorption positions of the adatoms above Al1 sites roughly correspond to the position of an Al atom if the Al_2O_3 structure were continued.

Diffusion Pathways

The minimum adsorption sites (i.e., the Al1 and Al2 sites) were used as initial and final locations of

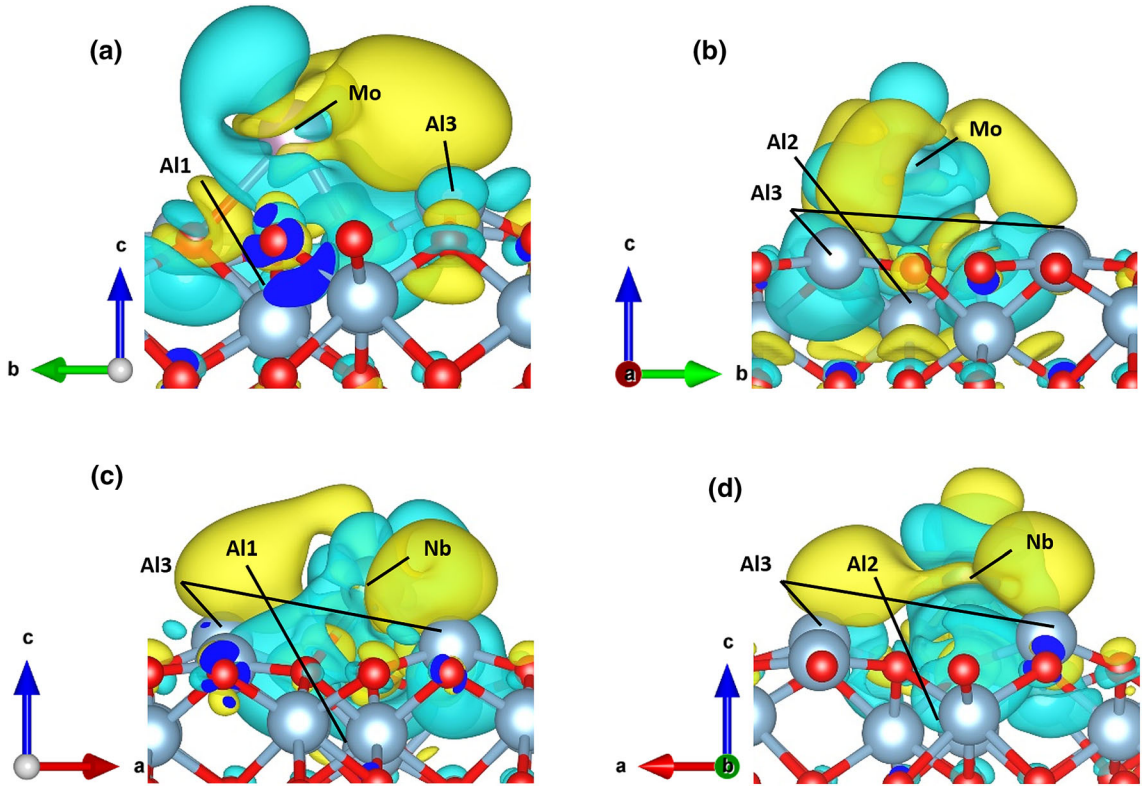

Fig. 2. Charge density differences of (a) Mo above an Al1 site, (b) Mo above an Al2 site, (c) Nb above an Al1 site, and (d) Nb above an Al2 site. Yellow zones represent an accumulation of electrons while blue zones represent a loss of electrons. Charge density differences were calculated using Eq. 2.

Table I. Minimum adsorption site energies in eV

Adatom	Al1 site	Al2 site
Mo	2.75	2.17
Nb	3.14	2.62

Al1 and Al2 sites are labeled in Fig. 1. Adsorption energies were calculated using Eq. 3. Large (more positive) values correspond to a stronger adatom-surface interaction

the adatoms for NEB calculations. It was assumed that the diffusion of adatoms occurred as hops between adsorption sites.[13–15] Two paths that connected minimum adsorption sites were considered for both Mo and Nb—a path connecting Al1 and Al2 sites (path 1) and a path connecting two Al1 sites (path 2). Due to the symmetry of the surface, the path from the Al2 to Al1 sites was assumed to be equivalent to path 1. From the single-image CI-NEB calculations, diffusion energy barriers were obtained for both paths.

Figure 3 shows the initial, final, and TS sites of the Mo and Nb adatoms along paths 1 and 2 while Fig. 4 exhibits corresponding diffusion energies for different sites. Frequency calculations were conducted to confirm minima and TS sites. Minima sites were confirmed because of the lack of imaginary frequencies. Saddle points for Mo path 2 and Nb paths 1 and 2 were also confirmed to be TS sites with the presence of a single imaginary frequency. No imaginary frequency was found at the saddle point for Mo path 1 and was therefore not considered a TS.

Path 1 for both Mo and Nb shown in Fig. 3a and c is similar, and the minima and saddle points are connected by a relatively straight line. Furthermore, the saddle points are located in nearly the same position—both about 2.20 Å from the minimum site, Al1. The energy barrier for the diffusion path connecting the Al1 and Al2 sites is 0.59 eV and 0.55 eV for Mo and Nb, respectively. However, since there is no imaginary frequency for the saddle point on the Mo path 1 (representing a Mo adatom at an Al2 site), it is not considered a TS site. The lack of imaginary frequency may be attributed to the flat potential energy surface near the saddle point and the local minimum—the energy difference between the saddle point and the local minimum (Al2 site) is 0.01 eV. For Nb path 1, the energy barrier for diffusion from Al2 to Al1 is slightly larger at 0.03 eV.

Path 2 for Mo is different from path 2 for Nb. The minimum sites and TS sites for Mo are connected by a relatively straight line, with the TS occurring above an O2 site, about 2.10 Å from the initial Al1 site. The diffusion energy barrier for Mo on path 2 is 0.47 eV, lower than that for path 1. Conversely,

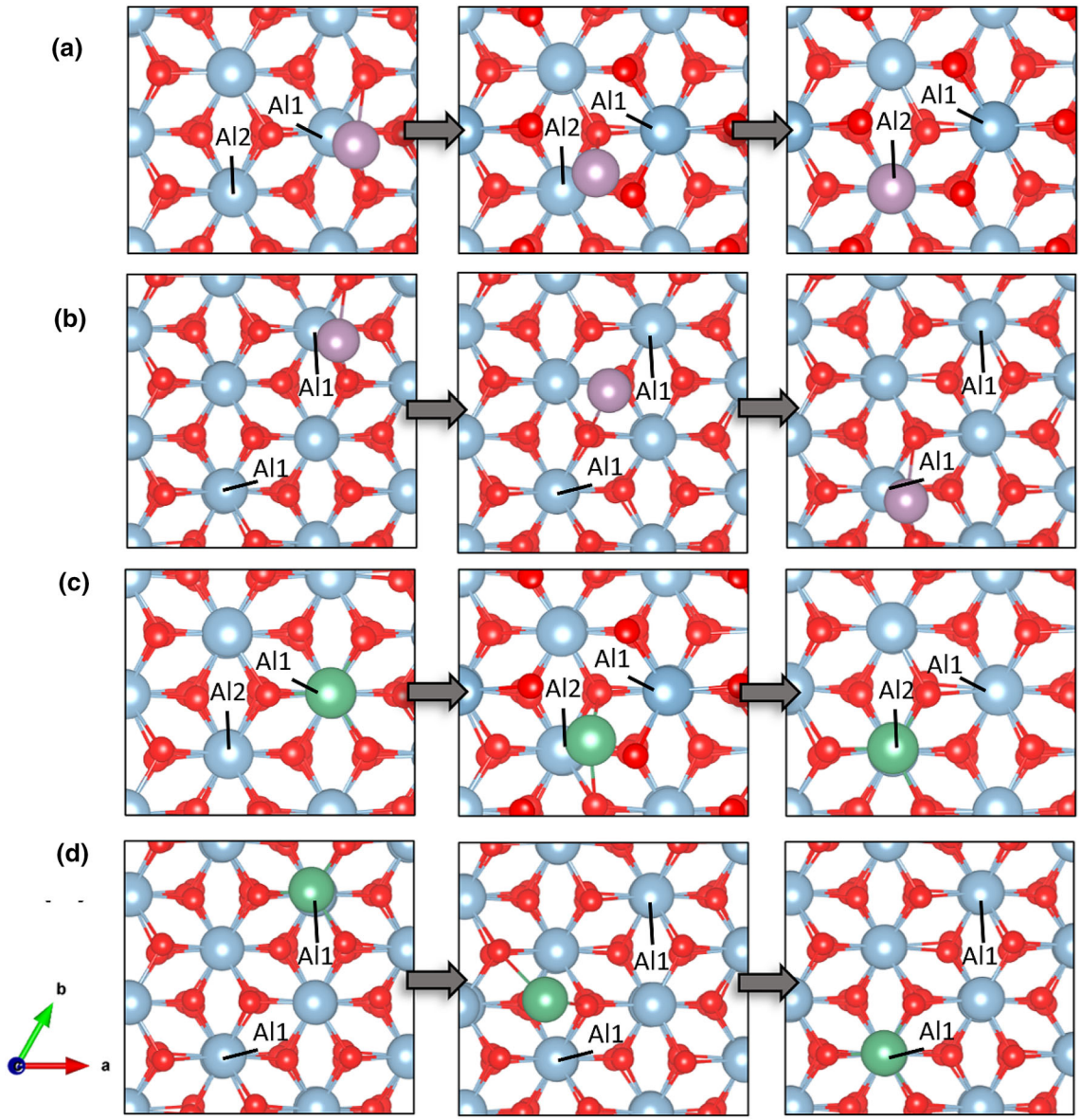

Fig. 3. (a) Mo diffusion path 1, (b) Mo diffusion path 2, (c) Nb diffusion path 1, and (d) Nb diffusion path 2. Blue atoms are Al, red atoms are O, purple atoms are Mo, and green atoms are Nb (Color figure online).

path 2 for Nb was found to be less linear and more curved than path 2 for Mo. The TS also occurs over an O2 site (labeled in Fig. 1) 3.75 Å from the initial Al1 site, and the barrier is larger than that of Mo at 0.87 eV.

Diffusion Coefficients

The diffusion energy barriers and vibrational frequency results were calculated to approximate the diffusion coefficients and pre-factors of the Mo and Nb adatoms. A detailed explanation of the procedure to estimate diffusion coefficients from CI-NEB calculations can be found in the literature,[10,11,14] and a brief summary is given here. The diffusion coefficient of an adatom on a surface can generally be given by the Arrhenius equation, as below:

$$D = D_0 \exp\left(-\frac{Q}{k_B T}\right) \tag{4}$$

where D_0 is the diffusion pre-factor, Q is the diffusion energy barrier, and T is temperature. The diffusion energy barrier is given by the difference between the minimum and maximum energies along the diffusion path, i.e.,

$$Q = E_{ts} - E_{min} \tag{5}$$

where E_{ts} is the energy of the diffusing adatom at the TS site, and E_{min} is the energy at a minima point. In similar systems, the zero-point energy

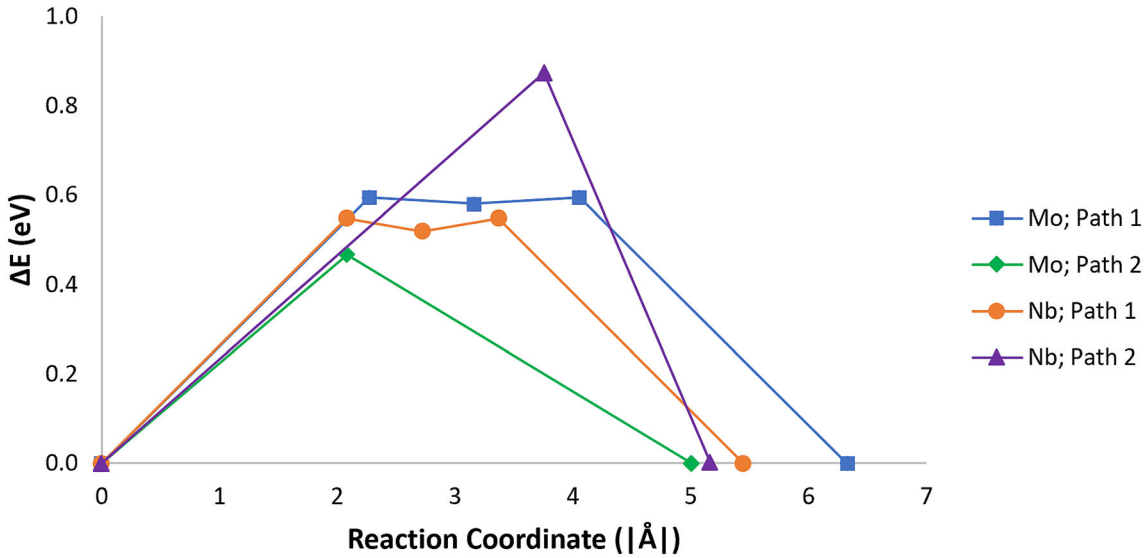

Fig. 4. Diffusion profiles determined from single-image CI-NEB calculations. Plots for diffusion path 1 were mirrored to show the entire path. The minimum energy points correspond to adatoms above Al1 sites. Local minima on path 1 correspond to adatoms above Al2 sites. Reaction coordinates calculated as the absolute distance from the initial adsorption position.

corrections are within ± 0.02 eV,[14] and so are neglected in Eq. 5. In the framework of transition state theory, D_0 can be estimated as

$$D_0 = \frac{l^2}{4}\frac{\prod_i^{3N} \nu_i^{\min}}{\prod_i^{3N-1} \nu_i^{TS}} \quad (6)$$

where l is the diffusion path length and ν are the normal modes of vibration. The value $3N$ corresponds to the number of normal modes for an adatom at a minimum site while $3N-1$ corresponds to the number of modes of an adatom at a TS site, because there is a single imaginary frequency at the TS site. The quantity $\frac{l^2}{4}$ accounts for the possible diffusion directions of an adatom on a hexagonal lattice surface. By combining Eqs. 4–6, the diffusion coefficient can be determined. In the case where adatom diffusion occurs in two steps, first order kinetics can be applied to write the total diffusion coefficient as

$$\frac{1}{D} = \frac{1}{D_1} + \frac{1}{D_2} \quad (7)$$

Using Eq. 7, the diffusion pre-factor can be found for a diffusion path with multiple steps. Results for D_0 and D are given in Table II at temperatures of 550 K, the approximate sintering temperature of printed metals,[2,22] and 1250 K, the maximum temperature at which printed melt wires were tested.[2]

As shown in Fig. 2, both Mo and Nb adatoms interact strongly with Al3 atoms. However, as shown in Fig. 4 and Table II, Mo path 2 has the lowest diffusion energy barrier compared to both Nb diffusion paths. The difference between energy barriers for Mo and Nb can be explained by the differences in their adsorption energies given in Table I, where Mo has a lower adsorption energy (2.75 eV at Al1 sites) than Nb (3.14 at Al1 sites), resulting in a weaker adatom-surface interaction. D_0 values were calculated using Eq. 6. The D_0 for Nb path 1 was calculated using Eq. 7 in combination with Eqs. 4 and 6 at a temperature of 1250 K (the D_0 at 550 K was found to be 8.05×10^{-8} m^2/s). In general, the calculated D_0 values are similar for both Mo and Nb, while Mo path 2 has the relatively larger value. The combination of low Q and larger D_0 leads to the largest overall D for Mo in Table II. Despite the smaller D_0 value calculated for Nb path 1, the value of D for Nb path 1 is larger than that of path 2 because of the larger Q of path 2. The calculated D value for Mo path 2 at 550 K is two orders of magnitude larger than Nb path 1 and four orders of magnitude larger than Nb path 2. At 1250 K, however, the differences in D between Mo and Nb are reduced. This might be attributed to the larger diffusion energy barriers for Nb, which could be more easily overcome at the higher temperatures.

DISCUSSION

Adsorption energy calculations revealed that Mo and Nb preferentially adsorb to similar sites on the Al_2O_3 (0001) surface and that the Nb adsorption energy is larger than that of Mo. They both interact strongly with Al3 surface atoms as opposed to subsurface Al atoms. However, we found some differences upon the adsorption of Mo and Nb adatoms. First, the Nb adatoms relaxed closer to the surface by about 0.1 Å above Al1 sites 0.3 Å above Al2 sites. Second, the Al atoms directly under the adatoms at the Al1 and Al2 sites moved downwards into the bulk region by about 0.07 Å further for Nb adsorption compared to Mo. Third,

Table II. Diffusion energy barriers (Q), calculated frequencies, diffusion pre-factors (D_0), and diffusion coefficients (D) calculated at 550 K and 1250 K

System	Q (eV)	Frequencies (cm^{-1})	D_0 (m^2/s)	D (m^2/s) @ 550 K	D (m^2/s) @ 1250 K
Mo; path 2	0.47	Al1: 222, 117, 69 TS: 137, 45, 49i	5.47×10^{-7}	2.95×10^{-11}	7.24×10^{-9}
Nb; path 1	0.55 (0.03)	Al1: 235, 155, 142 Al2: 223, 142, 121 TS: 230, 155, 37i	7.97×10^{-8}	7.70×10^{-13}	4.93×10^{-10}
Nb; path 2	0.87	Al1: 235, 155, 142 TS: 222, 178, 30i	2.62×10^{-7}	2.60×10^{-15}	7.88×10^{-11}

In the case of two-step diffusion, the secondary Q is given in parentheses. Mo path 1 is neglected because of the lack of imaginary frequencies at the saddle point. D_0 for Nb path 1 was calculated using 1250 K

upon adsorption above Al1 sites, charge was found to be transferred between the Mo adatom and a single Al3 atom, while Nb was found to exchange charge with two Al3 atoms. Upon adsorption above Al2 sites, charge was found to be transferred between the Mo adatom and three Al3 atoms, while Nb was again found to exchange charge with two Al3 atoms. Furthermore, CI-NEB results suggested that two diffusion paths are available for both Mo and Nb—a path connecting two Al1 sites (path 1) and another path connecting Al1 and Al2 sites (path 2). However, no imaginary frequency was found for the saddle point of Mo path 1, which was therefore not considered for diffusion coefficient calcualtions. This is likely due to the flat potential energy surface, where the energy difference between the saddle point and the Al2 minima site is only 0.01 eV. Conversely, path 2 for Mo and path 1 and path 2 for Nb are identified as TS structures with imaginary frequencies for the saddle points. The larger diffusion energy barrier for Nb can be attributed to its larger adsorption energy, leading to smaller diffusion coefficients than those for Mo. Compared with other studies,[14,39] the diffusion pre-factors of Mo and Nb are between those of Al (fast diffusion) and Hf, Y, and Pt (slower diffusion). Furthermore, Mo and Nb have activation energy barriers close to those of Al and Pt.[14] The surface diffusion rates of Mo and Nb adatoms are estimated to be similar to those of Al adatoms because of their similar diffusion pre-factors and energy barriers.

In the case where Mo and Nb may be printed together (as is done for HTIR-TCs[18]), the preference for Mo and Nb to occupy the same sites (Al1 and Al2) and the larger Mo diffusion coefficients may cause competition for adsorption sites among the adatoms (i.e., site blocking). Surface diffusion coefficients may also impact the spreading of the printed material on a substrate.[40–42] For example, upon heating Mo and Nb metals on a substrate, the difference in diffusion coefficients means the Mo adatoms may diffuse (spread) on the surface more quickly than Nb adatoms.[43] However, this is mitigated at higher temperatures because of the smaller differences between their diffusion coefficients. Finally, diffusion coefficients can also be used for the development of the larger scale phase-field models of the advanced manufacturing process of metal devices.[44,45]

CONCLUSION

The adsorption and diffusion of Mo and Nb adatoms on the α-Al_2O_3 (0001) surface were explored using density functional theory-based methods. The energies of three different surfaces terminated with Al′, Al, and O layers were calculated. We found the Al′-terminated one as the most energetically stable surface. Adsorption energy calculations were conducted using Mo and Nb adatoms initialized at five high-symmetry sites above the surface. Both Mo and Nb were preferentially relaxed to be above sub-surface Al sites. Using the minimum adsorption sites as starting and ending locations for the diffusion paths, NEB calculations were also conducted to find approximate minimum energy pathways between energetically minimum sites. Using the approximate paths as inputs, CI-NEB calculations were performed to find diffusion energy barriers. A single TS path exists for Mo while two possible TS paths exist for Nb. It was found that Mo and Nb follow similar diffusion paths, which may lead to site blocking. The calculated surface diffusion pre-factors of Mo and Nb were found to be similar; however, it was determined that the diffusion coefficients of Mo are larger because of a smaller diffusion energy barrier. The differences in diffusion coefficients may affect how the Mo and Nb metals spread on the substrate when printed together (e.g., Mo may spread quicker than Nb because of its larger diffusion coefficient). The results presented in this study provide detailed insight into the printing of metal systems, the understanding of which is crucial for the development and optimization of advanced manufacturing processes.

CONFLICT OF INTEREST

On behalf of all authors, the corresponding author states that there is no conflict of interest.

ACKNOWLEDGEMENTS

We thank Dr. Michael McMurtrey and Dr. Joseph Bass at the Idaho National Laboratory for their insightful discussions about advanced manufacturing materials and methods. This work was supported in part through the Department of Energy Advanced Sensors and Instrumentation program under DOE Idaho Operations Office Contract DE-AC07-05ID14517. The views and opinions of authors expressed herein do not necessarily state or reflect those of the US Government or any agency thereof. This research made use of Idaho National Laboratory computing resources, which are supported by the Office of Nuclear Energy of the US Department of Energy and the Nuclear Science User Facilities under Contract No. DE-AC07-05ID14517.

OPEN ACCESS

REFERENCES

1. J. Tran-Gia, S. Schlögl, and M. Lassmann, *J. Nucl. Med.* 57, 1998. (2016).
2. K. Mondal, K. Fujimoto, and M.D. McMurtrey, JOM 1 (2020).
3. J. Mathew, C. Hauser, P. Stoll, C. Kenel, D. Polyzos, D. Havermann, W.N. Macpherson, D.P. Hand, C. Leinenbach, A. Spierings, K. Koenig-Urban, and R.R.J. Maier, *IEEE Sens. J.* 17, 4107. (2017).
4. X. Lou, and D. Gandy, JOM 71, 2834. (2019).
5. R.P. Gandhiraman, V. Jayan, J.W. Han, B. Chen, J.E. Koehne, M. Meyyappan, and M. Meyyappan, *ACS Appl. Mater. Interfaces* 6, 20860. (2014).
6. K. Mondal, and M.D. McMurtrey, *Mater. Today Chem.* 17, 100328. (2020).
7. A.C. Kandemir, D. Erdem, H. Ma, A. Reiser, and R. Spolenak, *Nanotechnology* 27, 135303. (2016).
8. F. Ruffino, G. Cacciato, and M.G. Grimaldi, *J. Appl. Phys.* 115, 084304. (2014).
9. Y. Wu, Z. Wang, P.F. Liu, T. Bo, C. Hao, C. Hu, Z. Cheng, B.T. Wang, and H. Zhou, *Phys. Chem. Chem. Phys.* 21, 17538. (2019).
10. S.S. Naghavi, V.I. Hegde, and C. Wolverton, *Acta Mater.* 132, 467. (2017).
11. C.D. Versteylen, N.H. Van Dijk, and M.H.F. Sluiter, *Phys. Rev. B* 96, 094105. (2017).
12. Y.J. Zhang, J.H. Lan, C.Z. Wang, Q.Y. Wu, T. Bo, Z.F. Chai, and W.Q. Shi, *J. Phys. Chem. C* 119, 5783. (2015).
13. J. Chapman, R. Batra, B.P. Uberuaga, G. Pilania, and R. Ramprasad, *Comput. Mater. Sci.* 158, 353. (2019).
14. I. Milas, B. Hinnemann, and E.A. Carter, *J. Mater. Chem.* 21, 1447. (2011).
15. Y. Tiwary, and K.A. Fichthorn, *Phys. Rev. B* 81, 195421. (2010).
16. W. Wu, X. Lei, S. Zhong, B. Sun, and C. Ouyang, *Appl. Surf. Sci.* 531, 147263. (2020).
17. A.J. Palmer, R.S. Skifton, M. Scervini, D.C. Haggard, and W.D. Swank, *EPJ Web Conf.* 225, 04010. (2020).
18. J. Daw, J. Rempe, D. Knudson, J. Crepeau, and S. C. Wilkins, in *6th Am. Nucl. Soc. Int. Top. Meet. Nucl. Plant Instrumentation, Control. Human-Machine Interface Technol.* 2009 **3**, 1769 (2009).
19. E. Sikorski, R. Skifton, and L. Li, Unpublished Research, Boise State University (2020).
20. K. Bong Goo, J.L. Rempe, J.F. Villard, and S. Solstad, *Nucl. Technol.* 176, 155. (2011).
21. J.L. Rempe, D.L. Knudson, K.G. Condie, and S.C. Wilkins, *Nucl. Technol.* 156, 320. (2006).
22. A. Delage, N. Delhote, S. Verdeyme, B. Bonnet, L. Carpentier, C. Schick, T. Chartier, and C. Chaput, in *IEEE MTT-S Int. Microw. Symp. Dig.* (Institute of Electrical and Electronics Engineers Inc., 2018), pp. 1557–1560.
23. R. Soukup, J. Navratil, J. Reboun, and T. Rericha, in *Proc. Int. Spring Semin. Electron. Technol.* (IEEE Computer Society, 2015), pp. 30–35.
24. A.A. Vasiliev, A.V. Sokolov, A.V. Legin, N.N. Samotaev, K.Y. Oblov, V.P. Kim, S.V. Tkachev, S.P. Gubin, G.N. Potapov, Y.V. Kokhtina, and A.V. Nisan, *Procedia Eng.* 120, 1087. (2015).
25. G. Kresse, and J. Furthmüller, *Comput. Mater. Sci.* 6, 15. (1996).
26. G. Kresse, and J. Furthmüller, *Phys. Rev. B Condens. Matter Mater. Phys.* 54, 11169. (1996).
27. P.E. Blöchl, *Phys. Rev. B* 50, 17953. (1994).
28. G. Kresse, and D. Joubert, *Phys. Rev. B Condens. Matter Mater. Phys.* 59, 1758. (1999).
29. J.P. Perdew, K. Burke, and M. Ernzerhof, *Phys. Rev. Lett.* 77, 3865. (1996).
30. S. Alavi, D.C. Sorescu, and D.L. Thompson, *J. Phys. Chem. B* 107, 186. (2003).
31. J. Sun, T. Stirner, and A. Matthews, *Surf. Coat. Technol.* 201, 4205. (2006).
32. J. Zhong, *Adhesives—Applications and Properties* (InTech, Rijeka, 2016), pp 363–387.
33. G. Henkelman, B.P. Uberuaga, and H. Jónsson, *J. Chem. Phys.* 113, 9901. (2000).
34. W.C. Mackrodt, *Phys. Chem. Miner.* 15, 228. (1988).
35. H.-T. Li, L.-F. Chen, X. Yuan, W.-Q. Zhang, J.R. Smith, and A.G. Evans, *J. Am. Ceram. Soc.* 94, s154–s159. (2011).
36. S. Blonski, and S.H. Garofalini, *Surf. Sci.* 295, 263. (1993).
37. S. Sun, P. Xu, B. Ma, H. Shang, and G. Li, *Comput. Mater. Sci.* 157, 37. (2019).
38. J.M. McHale, A. Auroux, A.J. Perrotta, and A. Navrotsky, *Science (80-)* 277, 788. (1997).
39. N. Aaron Deskins, D. Mei, and M. Dupuis, *Surf. Sci.* 603, 2793. (2009).
40. E. Saiz, C.W. Hwang, K. Suganuma, and A.P. Tomsia, *Acta Mater.* 51, 3185. (2003).
41. M. Geissler, H. Wolf, R. Stutz, E. Delamarche, U.-W. Grummt, B. Michel, and A. Bietsch, *Langmuir* 19, 6301–6311. (2003).
42. H. Bettermann, M. Werner, and M. Getzlaff, *Appl. Surf. Sci.* 391, 49. (2017).
43. J. Pstruś, *J. Mater. Sci. Mater. Electron.* 29, 20531. (2018).

44. K. Chockalingam, V.G. Kouznetsova, O. van der Sluis, and M.G.D. Geers, *Comput. Methods Appl. Mech. Eng.* 312, 492. (2016).
45. L.K. Aagesen, Y. Gao, D. Schwen, and K. Ahmed, *Phys. Rev. E* 98, 023309. (2018).